Objective Analysis of ARM IOP Data: Method and Sensitivity

M. H. ZHANG AND J. L. LIN

State University of New York at Stony Brook, Stony Brook, New York

R. T. CEDERWALL, J. J. YIO, AND S. C. XIE

Lawrence Livermore National Laboratory, Livermore, California

(Manuscript received 11 June 1999, in final form 5 July 2000)

ABSTRACT

Motivated by the need to obtain accurate objective analysis of field experimental data to force physical parameterizations in numerical models, this paper first reviews the existing objective analysis methods and interpolation schemes that are used to derive atmospheric wind divergence, vertical velocity, and advective tendencies. Advantages and disadvantages of different methods are discussed. It is shown that considerable uncertainties in the analyzed products can result from the use of different analysis. The paper then describes a hybrid approach to combine the strengths of the regular grid and the line-integral methods, together with a variational constraining procedure for the analysis of field experimental data. In addition to the use of upper-air data, measurements at the surface and at the top of the atmosphere (TOA) are used to constrain the upper-air analysis to conserve column-integrated mass, water, energy, and momentum.

Analyses are shown for measurements taken in the Atmospheric Radiation Measurement Program July 1995 intensive observational period. Sensitivity experiments are carried out to test the robustness of the analyzed data and to reveal uncertainties in the analysis. These include sensitivities to the interpolation schemes, to the types of input data sources, and to the variational constraining procedures. It is shown that the constraining process of using additional surface and TOA data significantly reduces the sensitivity of the final data products.

1. Introduction

Deriving atmospheric wind divergence, vertical velocity, and advective tendencies from field experimental data is an old topic. It gained renewed attention in recent years because of the need to use these derived quantities to force and evaluate physical parameterizations in general circulation models (GCMs) (Randall et al. 1996). The setups of two recent major field experiments have all aimed to force model parameterizations with observed data. These are the Tropical Ocean and Global Atmosphere Coupled Ocean–Atmospheric Response Experiment (TOGA COARE) and the Atmospheric Radiation Measurement (ARM) Program of the Department of Energy (Webster and Lukas 1992; Stokes and Schwartz 1994). Most parameterized processes, such as cumulus convection and clouds, occur on timescales shorter than a day. In order to meaningfully interpret model results of these processes against observations, accurate forcing data of high temporal resolution are needed.

The main problem in deriving accurate objective analysis from a field experiment is the insufficient sampling of measurements, attributed not only to invalid or missing measurements, but also to scale aliasings. The actual measurements contain information of all scales including those that the observational network cannot resolve. Thus, it is not always appropriate to directly use point measurements to extract area-mean quantities. Limitation in the accuracy of instruments and measurements is another source of concern. When a field experiment is conducted in a small region, instrument and measurement errors can have a large impact on the derivative fields. The significant challenges to the objective analysis of field data have been highlighted in the recent studies of Mace and Ackerman (1996) and Parsons and Dudhia (1997), who conducted observating system simulation experiments to show potential large errors in objectively analyzed data.

For the Global Atmosphere Research Experiment (GARP) Atlantic Tropical Experiment (GATE), after its completion in 1974, Ooyama made a 5-yr concentrated effort to derive the objective analysis (Ooyama 1987). For TOGA COARE, Lin and Johnson (1996a,b) used several methods to analyze sounding measurements.

Corresponding author address: Dr. Minghua Zhang, Institute for Terrestrial and Planetary Atmospheres, State University of New York at Stony Brook, Stony Brook, NY 11794-5000.
E-mail: mzhang@notes.cc.sunysb.edu

They tested linear and quadratic fitting methods and concluded that the methods were not suitable due to the uneven distribution of COARE stations. They used the Barnes interpolation scheme in the final analysis (Barnes 1964). The cubic-spline mechanical fitting package described in Ooyama (1987) was also tested. It was concluded that the results are similar to those from the Barnes analysis. Frank et al. (1996) also analyzed the TOGA COARE data but used the line-integral method. Moisture budget from their analysis is very different from that in Lin and Johnson. For example, the intensive observational period (IOP) mean of diagnosed precipitation is 10.5–11.8 mm day^{-1} in Frank et al. versus 5.7–6.1 mm day^{-1} in Lin and Johnson. This magnitude of uncertainty is likely to be typical of most existing objective analyses. Uncertainties in the transient data are even larger. The possible impact of errors in the analyzed data on the model simulations has been shown in Ghan et al. (2000) for ARM and Krueger and Lazarus (1999) for TOGA COARE. Continued efforts are therefore required to improve these analyses.

This paper describes an objective analysis scheme for ARM. We first review several commonly used methods and schemes, and highlight their strengths and weaknesses. We then introduce a hybrid approach of combining the regular-grid method and the line-integral method in conjunction with a variational constraining procedure (Zhang and Lin 1997). The constraining procedure uses additional surface and top-of-the-atmosphere (TOA) measurements to assure consistencies in the objective analysis. We finally carry out sensitivity experiments to examine the robustness of our data.

The paper is organized in the following order. Section 2 reviews the commonly used objective analysis methods. Section 3 introduces the hybrid approach and describes the implementation of the variational constraining procedure for the July 1995 ARM IOP data. Section 4 presents the sensitivity study. The last section contains a summary of the paper.

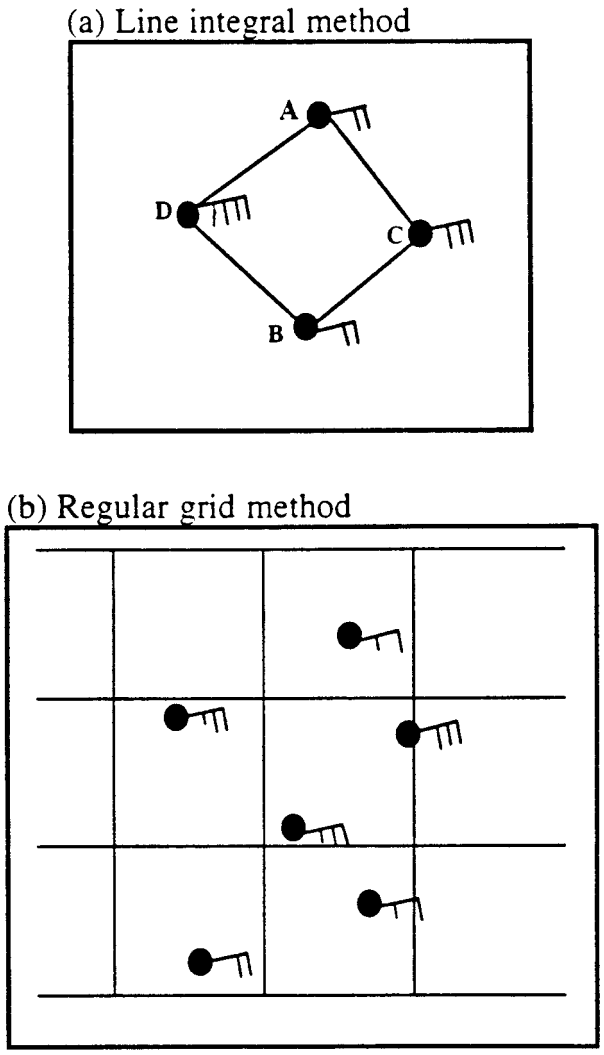

FIG. 1. Schematic figure of the line-integral approach vs the regular-grid method.

2. A review of commonly used objective analysis methods

Methodologically, horizontal derivatives, when averaged over a field experimental domain, can be calculated using three possible approaches that we will call analytical, line-integral, and finite-difference methods. The first method uses an assumed functional form of the spatial distribution of a field. The least square fitting of this function to the observed data is used to derive the unknown coefficients in the function. Spatial derivatives can then be analytically evaluated. We call this approach the fitting method. The second method uses line integrals of fluxes passing through the boundary of a selected domain to calculate the area-averaged divergence field. The linear assumption is often used in the calculation of the fluxes through two stations (Fig. 1a). The third method consists of establishing regularly spaced grid points, interpolating or extrapolating observational data to these regular grids, and then taking the standard finite difference of the interpolated fields. We refer this technique as the regular-grid method (Fig. 1b).

Technical implementation of the fitting and line-integral methods are rather straightforward. With three stations, Davies-Jones (1993) showed that linear fitting and line-integral calculation of the divergence fields are exactly the same. With more stations, results from these two methods differ because of their different assumptions, one being a prescribed functional form within the analysis domain, and the other being only related to observations at the domain boundary. A key element in the fitting method is the choice of the functional form, which can be quite subjective. There is no magic prescription for this form. For example, Thompson et al. (1979) experimented with both linear and quadratic fit-

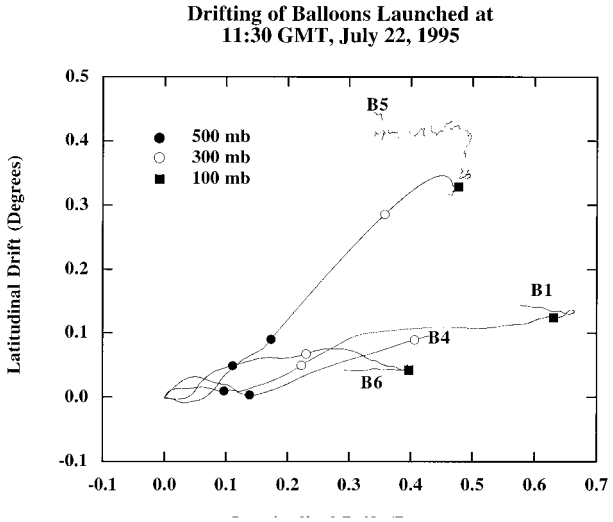

FIG. 2. Drifting location of balloons, relative to the ground stations, launched at the four ARM boundary facilities (B1, B4, B5, B6) at 1130 UTC 22 Jul 1995.

ting in their analysis of the GATE data, while Ooyama (1987) used cubic-spline fitting.

With the line-integral approach, potential problems can arise from the relative locations of the adjoining stations. For example, if the analysis domain is triangle ABC in Fig. 1a, the flux calculation through boundary AB would only use measurements from stations A and B. Wind convergence would be inferred since the wind at C is stronger than those at A and B. In reality, however, measurement at D suggests that this region is most likely experiencing a wind divergence. This type of problem is not uncommon in field experiments because of logistical reasons. Differential drifting of balloons at different stations poses a similar problem. Figure 2 shows the drifting of balloons launched at around 1130 UTC on 22 July, 1995 at the four ARM Southern Great Plains (SGP) balloon facilities (their locations are shown in Fig. 4). Typical ascending time of a balloon from the surface to 200-mb level is about 1 h. With an averaged wind speed of 15 m s^{-1}, a balloon could have drifted over 50 km at that level. As shown in Fig. 2, the change of the relative position between two balloons could be as large as 0.2° in latitude and longitude, which is about 20% of the distance between two ground stations. An extreme scenario is that convergent winds move the balloons close to each other and divergent winds move the balloons away from each. Direct use of balloon measurements in the line-integral method, therefore, may introduce errors.

The regular-grid method deserves more discussion, not only because it is widely used in the literature, but also because this method is also used to fill missing data in the line-integral and fitting approaches. In comparison with the line-integral approach, the strength of the regular-grid method is that it can easily combine measurements from various platforms and from various stations. The weakness is that potential problems in the original measurements become hidden in the analysis. The main step in the regular-grid method is to interpolate measurements to the analysis grid points. The general form of the interpolation and extrapolation of a field f to a set of prescribed grid points can be written as

$$f_a(x_i) = f_b(x_i) + \sum_{k=1}^{k=K} w_{ik}[f_o(x_k) - f_b(x_k)], \quad (1)$$

where subscript a represents analyzed field at the N analysis grid points x_i ($i = 1, 2, \ldots, N$) and x_i is a three- or four-dimensional vector (when time is used). Subscript b represents a background field. If no background field is needed, f_b can be set to zero. Subscript o represents observational data, which are made at K stations at x_k ($k = 1, 2, \ldots, K$). Here, w_{ik} is the weighting coefficient of measurement at x_k for the analysis at x_i. Sometimes the calculation from Eq. (1) is considered as an estimate of the background field; the final analysis can then be iteratively obtained as

$$f_a^{(n+1)}(x_i) = f_a^{(n)}(x_i) + \sum_{k=1}^{k=K} w_{ik}[f_o(x_k) - f_a^{(n)}(x_k)], \quad (2)$$

where the superscript n represents the sequence of iteration. If the iteration is carried out up to the convergence of the solution, the second term on the right of Eq. (2) becomes zero, and the analyzed data matches observations at the measurement stations. This is often an undesirable feature because the true spatial variability of a field is never the same as what is implied by the spatial structures of the weighting coefficients, and measurement errors should be considered. The most widely used interpolation schemes in the literature are the Barnes scheme (Barnes 1964), the Cressman scheme (Cressman 1959), and the statistical interpolation scheme (e.g., Ooyama 1987).

In the Barnes scheme, the initial analysis is simply a weighting average of existing measurements. The weighting coefficients are calculated based on the distance between an analysis grid point and the measurement stations:

$$w_{ik} = w(x_i, x_k) = w_o \exp\left[-\frac{(x_i - x_k)^2}{L^2}\right],$$
$$\sum_k w_{ik} = 1, \quad (3)$$

where L is a prescribed length scale. All measurements are used for the analysis at each grid point. Calculation can be carried out regardless of the amount of available measurements. The drawback is that one or two available measurements can fill all grid points in the whole analysis domain. In the Barnes scheme, the weighting of observational data is blind to the actual location of the observational station other than the distance. As a consequence, if two stations are very close to each other,

such as a balloon sounding overlapping a profiler, measurements from that location would carry double weight.

The Cressman scheme (Cressman 1959) uses a weighting function of

$$w_{ik} = w(x_i, x_k) = \begin{cases} \dfrac{1}{N_i}\dfrac{L^2 - (x_i - x_k)^2}{L^2 + (x_i - x_k)^2}, & d_{ik} < L, \\ 0, & \text{otherwise} \end{cases} \quad (4)$$

where d_{ik} is the distance between an observation station and an analysis grid point. Here, N_i is the number of measurements within distance L of the analysis grid point x_i. A background field is required. Interpolation is carried out for the difference field between observations and the background, rather than the observation itself. If there is no measurement within the distance L of an analysis grid point, the scheme will only take the background field as the analysis.

The statistical interpolation scheme avoids the subjective specification of the weighting coefficients. The general form of the statistical interpolation is the same as Eq. (1). The time dimension is often used to form a statistical ensemble. The weighting coefficients are calculated based on the distribution of the covariance fields. They are obtained through the minimization of error variance described as

$$\varepsilon^2 = \left\langle \sum_{i=1}^{I} [f_a(x_i) - f(x_i)]^2 \right\rangle, \quad (5)$$

where $f(x_i)$ is the ''true'' field at the analysis grid point x_i. The bracket represents the ensemble average (time average). Without the use of a background field, the analysis is written as

$$f_a(x_i) = \sum_{k=1}^{k=K} w_{ik} f_o(x_k), \quad (6)$$

and the weighting coefficients are calculated as (Daley 1991)

$$\mathbf{M}\mathbf{w}_i = \mathbf{P}_i, \quad (7)$$

where $\mathbf{w}_i$ is the $K \times 1$ vector of weighting coefficients of the K measurements for the analysis at x_i. The matrix $\mathbf{M}$ is the $K \times K$ covariance matrix among observational stations, and $\mathbf{P}_i$ is the $K \times 1$ covariance vector of the true field at the analysis grid point x_i with all measurement stations x_k. This procedure is expected to discount the weighting of stations that are significantly correlated with each other. The difficult step in this analysis procedure is the calculation of the covariance field involving the true field. Some approximation of the true field is needed to obtain the covariances, which could be the analysis from the Barnes scheme, the Cressman scheme, or a background field directly.

The interpolation scheme used in Ooyama (1987) for GATE is a modification of the standard statistical algorithm. Ooyama (1987) considered that the true field contained undesirable small-scale features. He therefore minimized the error variance of the analysis with respect to a ''smoothed true field'' rather than the ''true field.'' A penalty function is used to measure the distance of the smoothed field and the true field. The cost function is written as

$$\varepsilon^2 = \left\langle \sum_{i=1}^{I} [f_a(x_i) - \overline{f}(x_i)]^2 \right\rangle + \left\langle \sum_{i=1}^{I} [\overline{f}(x_i) - f(x_i)]^2 \right\rangle, \quad (8)$$

where $\overline{f}$ is the smoothed true field. The actual calculation of the weighting coefficients is exactly the same as in the standard statistical method, except that the smoothed true field is used in the covariance calculation for $\mathbf{P}_i$. This is because the second term in (8) does not depend on the weighting coefficients. Ooyama used a cubic-spline fitting, with a penalty function to limit the magnitude of the horizontal derivatives, to obtain the smoothed true fields. Use of a smoothed field for the calculation of the covariance is one unique aspect of the Ooyama scheme.

The second unique aspect of the Ooyama scheme is to further filter available observations used in the weighted mean calculation of Eq. (6). At any given time, the spatial structure of the observations is expanded according to the empirical orthogonal functions (EOFs) of the covariance matrix, and only those components with significant contributions to the total variance of the field are retained. Ooyama (1987) showed this filtering to be also effective in desensitizing the statistical analysis. These two aspects, one modifying the weighting coefficients, and the other modifying the weighting data, both tend to smooth the analysis field.

To demonstrate the impact of these interpolation schemes on the analysis result, we use the analysis of the eastward component of the 500-mb wind at 1130 UTC 22 July 1995 at the ARM SGP site as an example. The input data are measurements from five balloons and 17 profilers. Figure 3a shows the Barnes analysis from the first iteration with length scale $L = 50$ km. The locations of the five ARM balloon facilities are labeled in the figure. The local impact of data at the B1 facility can be seen clearly in the figure. Figure 3b shows the same analysis except that the length scale is changed to 200 km. With this length scale, the analysis field is drastically smoothed. With the same length scale of $L = 200$ km, Fig. 3c shows the Barnes analysis after four iterations. The iteration regenerates smaller-scale features. Increasing the number of iterations is somewhat equivalent to reducing the length scale. The analysis from the Barnes procedure, as can be expected, is sensitive to the choice of the length scale and the number of iterations (Leach et al. 1996). By taking the difference of the analyzed field at two stations, say B1 and B6, one sees that the difference in the derivative field among the three analyses in Figs. 3a–c can be over 100% of the derivative field itself. These parameters have similar

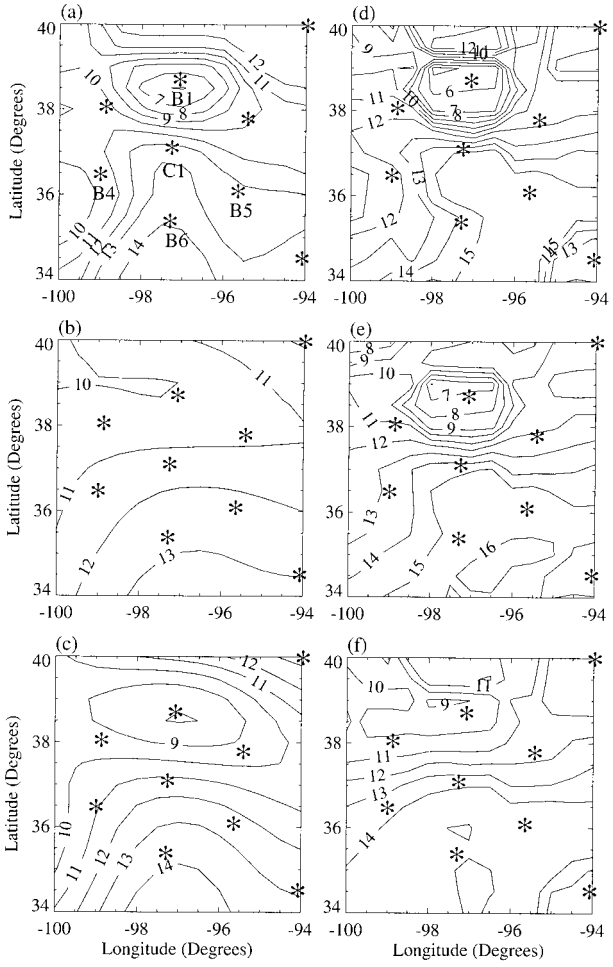

FIG. 3. Analysis of the eastward wind component (m s^{-1}). The five ARM balloon facilities are labeled (C1, B1, B4, B5, B6). The star denotes profiler stations within the plot domain. The Barnes scheme: (a) $L = 50$ km, one iteration; (b) $L = 200$ km, one iteration; (c) $L = 200$ km, four iterations; (d) standard statistical method; (e) with smoothed true field; and (f) with smoothed true field and filtered measurements.

impacts on the analysis from the Cressman scheme (not shown).

We next show results from the statistical schemes. Figure 3d shows analysis from the standard statistical interpolation, in which the Barnes analysis of Fig. 3c is used in the covariance calculation. It is seen that the analysis has not eliminated the small-scale structures associated with a low-value data point at B1. We next follow Ooyama (1987) and show in Fig. 3e the result when the true field is smoothed by a simple nine-point box averaging. The covariance vector is therefore slightly changed. It is seen that the analysis becomes smoother, owing to the change in the weighting coefficients. Figure 3f shows an analysis that further filters the observation by using only those EOF components that explain 95% of the total variance. It is seen that this step is effective in reducing the impact of the small local feature at B1, which is filtered out in the reconstruction of EOFs.

These calculations show that the final data product is sensitive to the analysis scheme and, perhaps, even more sensitive to the actual implementation of a particular scheme. Major advantages of using the Cressman and Barnes schemes are their mathematical simplicity, especially with the Barnes scheme where no background field is needed. A major weakness of both these schemes is the dependence of the calculation on the assumption of the length scale, the number of iterations, and their blindness to the actual locations of the observations other than the distance. Serious problems can occur when the stations are ill-positioned or when there are few measurements, and these problems are hidden to the users. In comparison with the Barnes and the Cressman schemes, the statistical scheme is more objective in the determination of the weighting coefficients. Weakness of this scheme is the subjectivity in the estimation of the covariances. Furthermore, a field experiment is often limited in length, and the sample size used in the correlation calculation is often small. Even if the sample is long, the actual data at the analysis time may not necessarily follow what is described by the correlation patterns.

An incomplete list of previous studies that have derived objective analysis from field experimental data is given in Table 1. Regardless of whether the regular-grid method or the line-integral approach and what interpolation schemes are used, the task at hand is often to derive data at grid points where no measurements or only aliased measurements are available. Given the above discussions, one has to conclude that there is a limit in the accuracy of objective analysis. After elaborate and in-depth discussion of the analysis of the GATE data, Ooyama (1987) concluded his paper with the quote ''to make gold, one must start with gold.''

3. A scheme used to analyze the ARM IOP data

The ARM program has two scientific objectives: 1) to improve the treatment of radiation processes in GCMs, and 2) to improve cloud parameterizations in these models (Stokes and Schwartz 1994). It is the second objective that requires the accurate knowledge of atmospheric dynamic structures at the ARM experimental test bed, including the vertical velocity and advective tendencies. Observed vertical velocity and advective tendencies are needed to force GCM physical parameterizations and single-column models (Randall et al. 1996; Ghan et al. 2000). The ARM SGP site has been in operation for several years. This section outlines an analysis scheme designed for ARM and discusses the implementation of the scheme for the analysis of the July 1995 ARM IOP data.

Figure 4a shows the five ARM balloon facilities at the SGP. Figure 4b shows the locations of the nearest seven National Oceanic and Atmospheric Administra-

TABLE 1. Previous objective analyses of large-scale vertical velocity and advective tendencies.

Asian monsoon		North America	
FGGE IIb	Luo and Yanai (1984)	Oklahoma squall line	Lewis (1975)
FGGE IIb	He et al. (1987)	Oklahoma	Sanders and Emanuel (1977)
QXPMEX	Yanai and Li (1994)	Florida	Johnson (1976)
1981 flood catastrophe	Kuo et al. (1986)	NHRE	McNab and Betts (1978)
WMONEX	Johnson and Young (1983)	SESAME	Kuo and Anthes (1984a,b)
TAMEX	Johnson and Bresch (1991)	SESAME	Wu and Yanai (1994)
TAMEX	Chen and Lin (1995)	OK PRE-STORM	Gallus and Johnson (1991, 1992)
TAMEX	Jorgensen et al. (1991)	OK PRE-STORM	Wu (1993)
TAMEX	Lin et al. (1990)	OK PRE-STORM	Lin and Johnson (1994)
		MCC composite	Cotton et al. (1989)
		CCOPE	LeMone and Moncrieff (1994)
Eastern Atlantic		Western Atlantic	
GATE III	Nitta (1977)	BOMEX	Nitta and Esbensen (1974)
GATE III	Thompson et al. (1979)		Esbensen (1975)
GATE III	Frank (1979)		
GATE I-III	Song and Frank (1983)		
GATE III	Ooyama (1987)		
GATE III	Esbensen et al. (1982)		
GATE	LeMone (1983)		
	LeMone et al. (1984)		
GATE	Sui and Yanai (1986)		
Western Pacific		South Pacific	
Marshall Islands	Reed and Recker (1971)	FGGE IIIb	Miller and Vincent (1987)
Marshall Islands	Nitta (1972)		
Marshall Islands	Yanai et al. (1973)		
TOGA COARE	Lin and Johnson (1996)		
TOGA COARE	Frank et al. (1997)		
Whole Tropics		Tropical cyclones	
FGGE IIIb	Pedigo and Vincent (1990)	Western Pacific composite	Lee (1989)
		Hurricane Debby	Lord and Franklin (1990)
Australian monsoon		South America	
AMEX	McBride et al. (1989)	VIMHEX	Betts (1973)
Africa			
COPT81	Lafore et al. (1988)		

AMEX—Australian Monsoon Experiment. BOMEX—Barbados Oceanographic and Meteorological Experiment. CCOPE—Cooperative Convective Precipitation Experiment. COPT—Convection Profonde Tropicale. FGGE—First GARP Global Experiment. MONEX—Monsoon Experiment. NHRE—National Hail Research Experiment. OK PRE-STORM—Oklahoma–Kansas Preliminary Regional Experiment for STORM-Central. QXPMEX—Qinghai–Xizang Plateau Meteorology Experiment. SESAME—Severe Environmental Storm and Mesoscale Experiment. TAMEX—Taiwan Area Mesoscale Experiment. VIHMEX—Venezuelan International Meteorological and Hydrological Experiment.

tion (NOAA) profilers. It is seen that all five sounding stations actually overlap with the wind profilers. The objective analysis domain is better defined when the two additional NOAA profiler stations are used.

In our analysis, we use a hybrid method of combining the strengths of the regular-grid method and the line-integral method. The procedure is equivalent to the regular-grid method in that we interpolate observations to a set of prescribed grid points. It differs from the traditional regular-grid method in that we select the analysis grid points to be as close as possible to the original observational stations, so that an analysis grid point is never far away from a measurement station and thus the final analysis is somewhat transparent to the original input data. Furthermore, a line-integral method is used in the end to derive the fluxes out of or into the analysis domain.

We additionally take the liberty of placing one more grid point on each side of the analysis domain as shown in Fig. 4c. These auxiliary grid points are added to improve the linear assumption on the line segment at the boundary, making use of measurements at other profiler stations. A fixed pressure coordinate with vertical resolution of 50 mb is used in the current study. The 12 boundary grid points define our final analysis domain.

The original upper-air measurements from the five balloon stations and 17 NOAA profilers are analyzed using the Cressman scheme with a four-dimensional length scale of (50 km, 50 km, 50 mb, 6 h). Iteration is carried out for three times. The NOAA Rapid Update Cycle (RUC) analysis is used as our background, whose grids are shown in Fig. 4d. Since profiler winds are available only in height coordinates, atmospheric temperature and humidity (for the calculation of virtual temperature) are first analyzed using balloon soundings and RUC output at the profiler stations. Profiler wind measurements are then converted to pressure levels for subsequent analysis.

On top of this upper-air analysis at the 12 grid points,

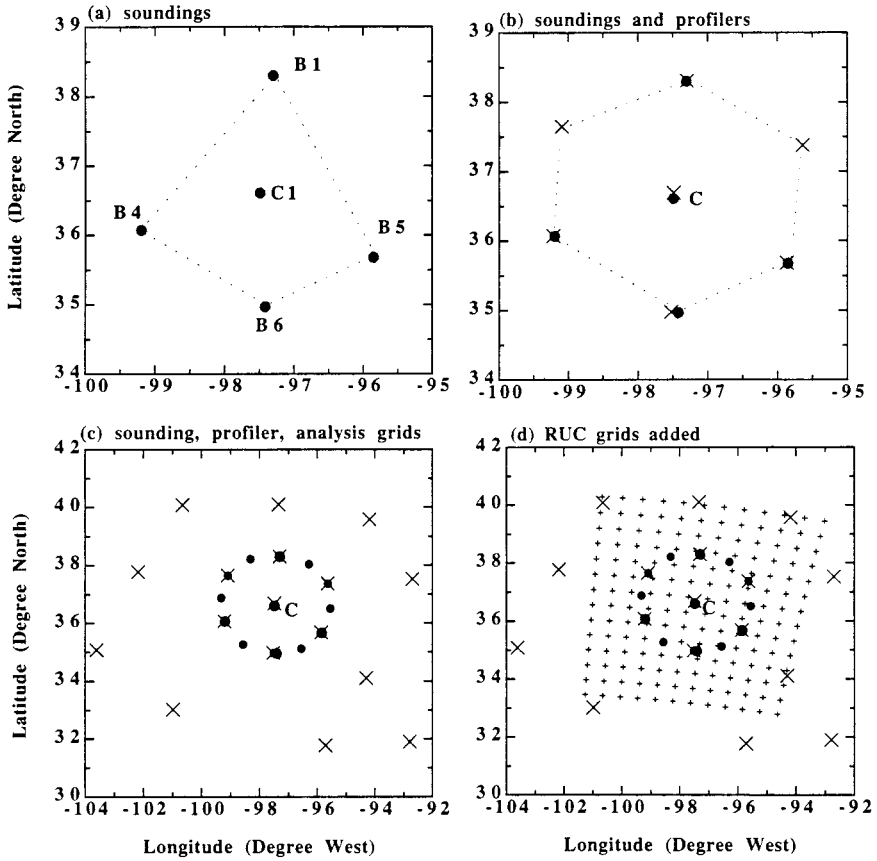

FIG. 4. Locations of the ARM upper-air data streams and the analysis grid points: (a) sounding stations, (b) seven profiler stations (crosses), and (c) the 12 analysis grid points (heavy dots) in the hybrid approach. Also plotted are the nearby profiler stations (crosses). (d) RUC grids overlaid on other grids.

we further constrain the upper-air data to be consistent with surface and satellite measurements. This is achieved by making minimum possible adjustments to the initial upper-air analysis at each grid point so that the final analysis yields column-integrated budgets of atmospheric mass, energy, water vapor, and momentum that are consistent with surface and TOA measurements. Therefore, whatever comes horizontally into the atmospheric column equals whatever comes out from the bottom and the TOA plus the increase of local storage of mass, energy, water vapor, and momentum. As described in the previous section, there is a limit in the accuracy of the initial upper-air analysis. Adjustment of this initial analysis is justified as long as its magnitudes are within the expected error bounds.

Technical details of this constrained variational step has been described in Zhang and Lin (1997). Zhang and Lin (1997) only used four balloons from the October 1994 ARM IOP data to illustrate the method. When applied to the present ARM data streams, the analysis is required to satisfy the following vertically integrated constraints:

$$\langle \nabla \cdot \mathbf{V} \rangle = -\frac{1}{g p_s} \frac{dp_s}{dt}, \tag{9}$$

$$\frac{\partial \langle q \rangle}{\partial t} + \langle \nabla \cdot \mathbf{V} q \rangle = E_s - \text{prec} - \frac{\partial \langle q_l \rangle}{\partial t}, \tag{10}$$

$$\frac{\partial \langle s \rangle}{\partial t} + \langle \nabla \cdot \mathbf{V} s \rangle = R_{\text{TOA}} - R_{\text{SRF}} + L\text{prec} + \text{SH} + \frac{\partial \langle q_l \rangle}{\partial t}, \quad \text{and} \tag{11}$$

$$\frac{\partial \langle \mathbf{V} \rangle}{\partial t} + \langle \nabla \cdot \mathbf{V}\mathbf{V} \rangle - f\mathbf{k} \times \langle \mathbf{V} \rangle - \nabla \langle \phi \rangle = \boldsymbol{\tau}_s, \tag{12}$$

where the bracket represents vertical integration, $\mathbf{V}$ is the wind, q is the water vapor mixing ratio, $s = CpT + gz$ is the dry static energy, and p_s is the surface pressure. Here, R is the net downward radiative flux at the TOA and at the surface (SRF); $\boldsymbol{\tau}_s$ is the surface wind stress, prec is the precipitation, SH is the sensible heat flux, E_s is the surface evaporation, and q_l is the cloud

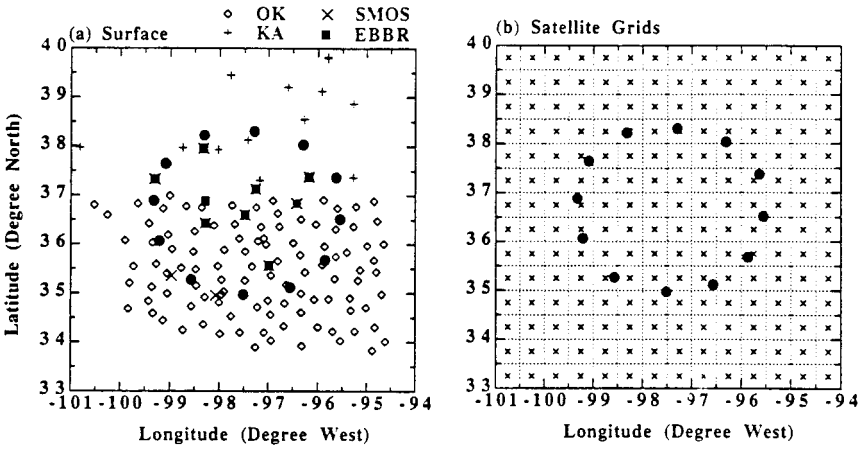

FIG. 5. (a) ARM surface data streams. See text for complete instrument names. (b) GOES grids over the analysis domain.

liquid water content. This is achieved by minimizing the following cost function:

$$I(t) = (\mathbf{u}^* - \mathbf{u}_o)^{\mathrm{T}}\mathbf{Q}_u(\mathbf{u}^* - \mathbf{u}_o) + (\mathbf{v}^* - \mathbf{v}_o)^{\mathrm{T}}\mathbf{Q}_v(\mathbf{v}^* - \mathbf{v}_o) + (\mathbf{s}^* - \mathbf{s}_o)^{\mathrm{T}}\mathbf{Q}_s(\mathbf{s}^* - \mathbf{s}_o) + (\mathbf{q}^* - \mathbf{q}_o)^{\mathrm{T}}\mathbf{Q}_q(\mathbf{q}^* - \mathbf{q}_o), \quad (13)$$

where subscript o in (13) denotes analysis from the initial interpolation schemes, superscript * denotes final analysis, and the $\mathbf{Q}$'s are the prescribed weighting functions. All variables on the rhs of Eq. (13) represent either vectors or matrices.

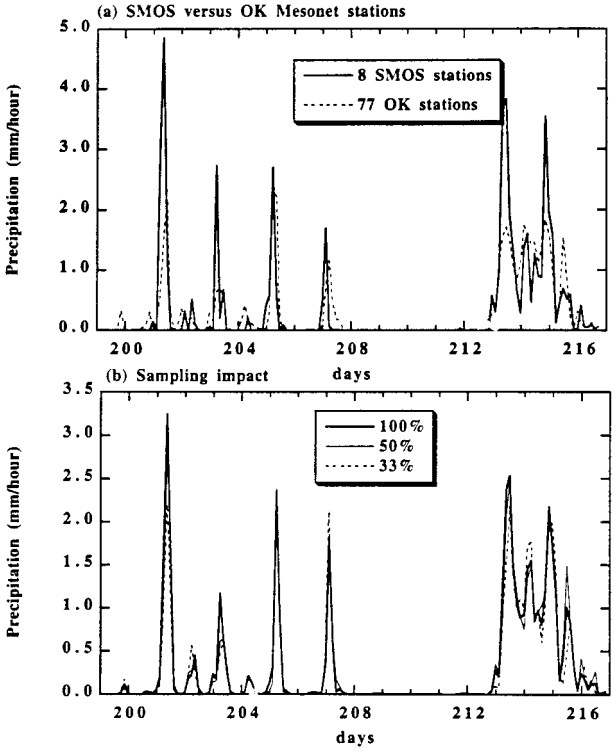

FIG. 6. Precipitation (mm h^{-1}): (a) eight SMOS stations and 77 Oklahoma and Kansas mesonet stations and (b) averaged gridded analysis with reduced number of stations.

Terms on the right-hand sides of Eqs. (9)–(12) are derived from surface and TOA measurements. Figure 5a shows a subset of ARM measurement platforms whose data are used. These include (i) the surface meteorological observational stations (SMOSs) that measure precipitation, surface pressure, winds, temperature, and relative humidity; (ii) the energy budget Bowen ratio (EBBR) stations that measure surface broadband net radiative flux and surface sensible and latent heat fluxes; (iii) the Oklahoma and Kansas mesonet stations measuring surface precipitation, pressure, winds, and temperature; and (iv) the microwave radiometer stations stations measuring precipitable water and total cloud liquid water. These stations overlap with the sounding stations and they are not separately plotted in the figure. Satellite measurements of clouds and broadband radiative fluxes are available from NASA Langley at half-hour frequency (Minnis et al. 1995). The 0.5° × 0.5° satellite grids are shown in Fig. 5b. Additional measurement platforms that are relevant to our objective analysis may be available for other IOPs. For example, for the 1997 summer ARM IOP, eddy correlation (ECOR) measurements of surface latent and sensible heat fluxes are available from the ECOR stations; and radar rainfall of 4 km × 4 km resolution covering the whole analysis domain is also available.

Sampling of surface measurements in calculating area-averaged quantities is a potential concern for variables that have large spatial variabilities such as precipitation. Figure 6a shows precipitation averaged over eight SMOS stations within the analysis domain, and that averaged over 77 Oklahoma and Kansas mesonet stations within the same domain. It is seen that they could differ by a factor of 2, with rainfall at the SMOS stations systematically larger than those from the mesonet stations. To reduce sampling biases, we lay the

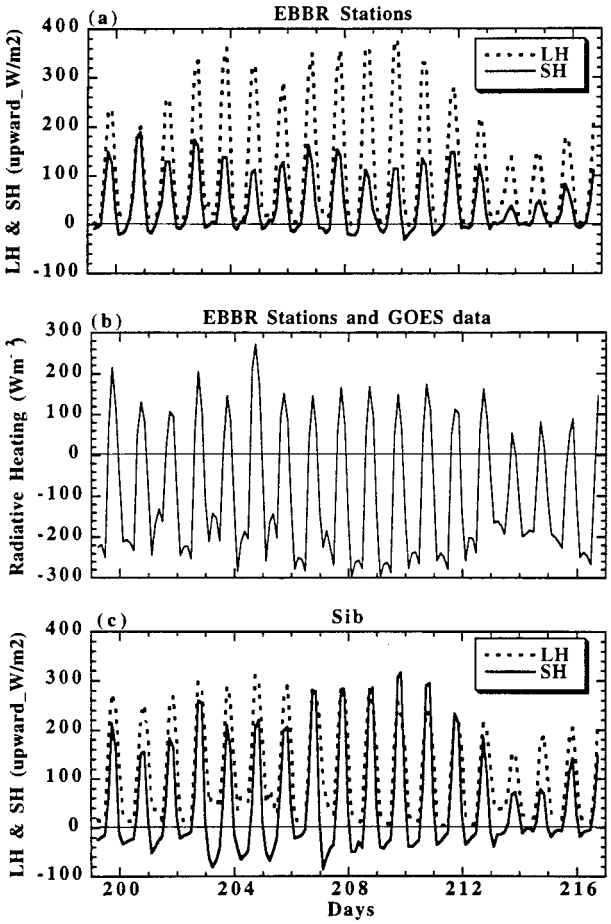

FIG. 7. Column-integrated fluxes: (a) surface latent and sensible heat fluxes (W m^{-2}), (b) radiative heating (W m^{-2}), and (c) surface latent and sensible heat fluxes from the Sib model.

0.5° × 0.5° Geostationary Operational Environment Satellite (GOES) grids in Fig. 5b over the analysis domain in Fig. 5a, and then derive the surface quantities in each small grid box. If there are actual measurements within a 0.5° × 0.5° grid box, simple arithmetic averaging is used to obtain the subgrid means. Some variables are available from several instruments. For example, surface winds are available from the sounding stations, the SMOS stations, and the Oklahoma and Kansas mesonet stations. They are merged in the arithmetic averaging process. If there is no actual measurement in a 0.5° × 0.5° box, then the Barnes scheme is used with the length scale of (Lx = 50 km, Ly = 50 km, Lt = 6 h) to fill the missing data. Missing broadband shortwave measurement is filled by applying this procedure to the albedo and then converting it to radiative flux. Domain averages of these quantities are obtained by using values from the 0.5° × 0.5° grid boxes within the analysis domain.

Figure 6b shows the area-averaged precipitation, calculated from this method, when all measurement stations are used, and when only half, as well as one-third, of the measurement stations are used. It is seen that the area-averaged precipitation asymptotes as the number of surface station increases to approach 50%, which is over 60 stations. All other constraint variables are calculated using the same procedure; this includes surface sensible and latent heat fluxes, column cloud liquid water content, radiative fluxes at surface, and TOA. Figure 7a shows the area-averaged surface latent and sensible heat fluxes. Figure 7b shows the atmospheric net radiative heating.

The variational procedure also requires the specification of error estimates to determine the weights in the cost function (13). It is the relative magnitudes of these estimates, rather than their absolute magnitudes, that enter into the minimization procedure. Zhang and Lin (1997) specified these weights according to instrument and measurement uncertainty estimates provided by the ARM instrument team (M. Wesley, Argonne National Laboratory, 1996, personal communication), which are 0.5 m s^{-1} for winds, 0.2 K for temperature, and 3% of the specific humidity. This specification has been recently modified to include a component that is related to the observed variance of atmospheric state variables in the sounding data. The standard deviations of the state variables are shown in Fig. 8. Variability of the winds generally increases with height, with the u component having larger variability than the v component. These standard deviations are multiplied by a factor of 20% to account for aliasing errors; they are then added to the instrument and measurement uncertainties used in Zhang and Lin (1997). As one can see, there is some degree of subjectivity in the selection of the error estimate. Sensitivity tests of the analysis will be presented.

4. Analysis of the July 1995 ARM IOP data and its sensitivity

The scheme described in the previous section, together with the surface and TOA measurements, is used to calculate the derivative fields for the July 1995 ARM IOP. This is the IOP for which a single-column modeling intercomparison has been carried out (Ghan et al. 2000). The IOP starts on 18 July 1995 and runs until 4 August 1995. The large-scale circulation over North America can be divided into three periods. In the beginning period from 17 to 28 July, a broad-bottomed trough extending from northern Canada covers most of the North America continent. The upper-air circulation over most of the United States is characterized by westerlies accompanying the bottom of the trough. The ARM SGP site is at the southern edge of this trough, and it is near the northern edge of the subtropical high. Weather conditions at the ARM site are therefore influenced by both the subtropical high and the middle-latitude circulations. It is under this large-scale circulation that several strong precipitation events, as seen in Fig. 6, took place.

The above circulation pattern remained stable for over a week, and then it was disrupted by a developing ridge

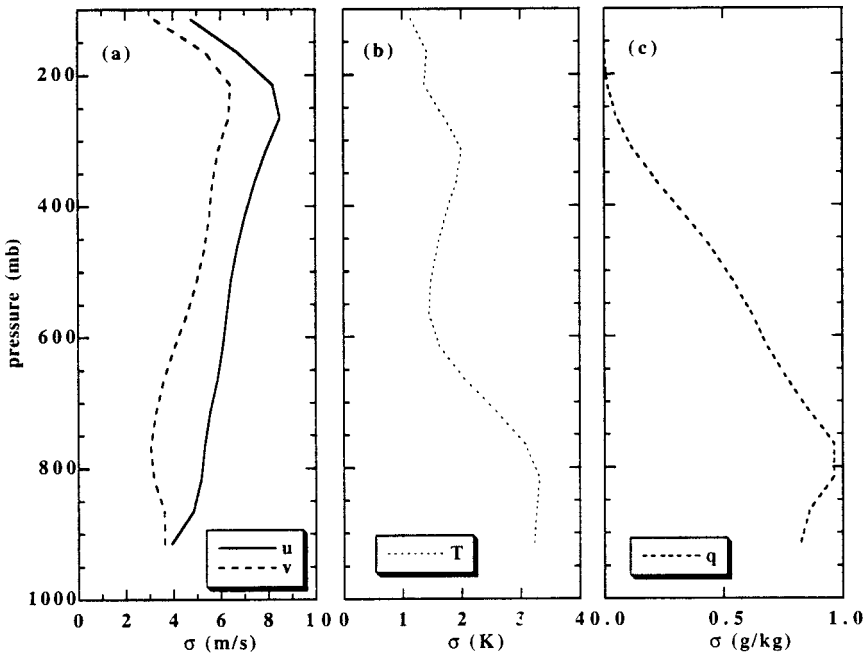

FIG. 8. Standard deviation of atmospheric variables as function of pressure: (a) u and v (m s^{-1}), (b) temp (K), and (c) water vapor mixing ratio (g kg^{-1}).

in the North Pacific that was further driven by a developing upstream trough starting from 26 July 1995 (day 207). This ridge next moved over the North America continent. Upper-level winds over the ARM SGP became southeastward. This period corresponds to the relatively quite period in Fig. 6.

The clear-sky period ended when the ridge moved out and the previously mentioned developing trough moved over the continent. Weather at the SGP was again under the control of a trough. This trough-controlled condition differed from the first period in that the bottom of the trough coincided with a tropical depression. Possibly because of this coincidence, the depression developed into a weak tropical hurricane. The ARM SGP was therefore located at the intersection of the middle-latitude trough and the tropical hurricane. Strong and continuous precipitation was observed (Fig. 6).

The mesoscale circulation over the ARM SGP is featured by the strong diurnal variation of lower-level winds that are confined below 800 mb. The lower-level jet often develops at the local evening, with wind blowing from southwest to northeast in the night. The wind direction turns gradually to align with the westerlies during the daytime. Associated with this change in the wind pattern, there is a strong diurnal variation of water vapor and temperature advections.

Figures 9a and 9b show the time–pressure cross sections of the analyzed temperature and water vapor mixing ratio. There are strong diurnal variations of temperature and water vapor near the surface below 850 mb. There is a general warming and drying in the second period when the atmospheric ridge is over the SGP. Other than these variations, the temperature field is relatively flat. The water vapor field is different; there are clear signatures of large variabilities in the upper-tropospheric moisture associated with the convective events.

At 99% of the grid points, the variational adjustments in winds, temperature, and relative humidity are less than 2 m s^{-1}, 1 K, and 5%, respectively. These adjustments are well within the uncertainties of measurements and interpolations. Yet, they have made a large impact on the derivative fields. This is understandable because of the relatively small size of the field experimental domain. Error of 1 m s^{-1} on top of a measurement value of 30 m s^{-1} is only about 3%. If it is divided by a horizontal distance of 100 km, the resulting error in the divergence field is 1.0×10^{-5} s^{-1}, which could be 100% of the divergence in a typical synoptic weather system.

The analyzed wind divergence and vertical velocity are shown in Figs. 9c and 9d, which are consistent with the surface and TOA measurements of energy and water fluxes. It is seen that episodes of strong upward motion occur in the first period, which are diurnally locked. There is overall downward motion starting around 25 July (day 206). The last period corresponds to relatively uniform upward motion. The transition altitude of wind convergence to wind divergence is higher for the episodic convective events than that for the continuous precipitation period, at about 350 mb versus about 450 mb. This altitude is where the upward motion peaks.

Attribution of the observed changes of temperature and moisture to the large-scale advection and Q1, Q2 (Yanai et al. 1973), and analysis of the contributions of

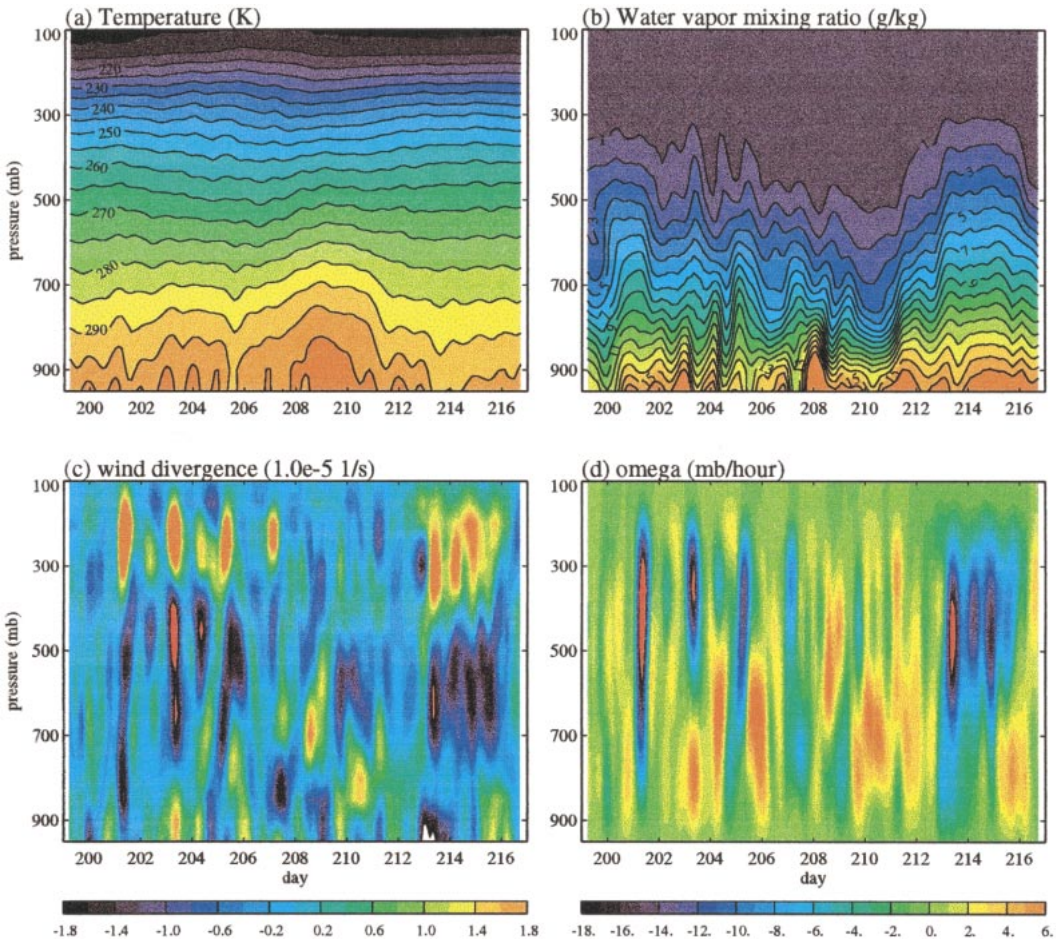

FIG. 9. Time–pressure distributions of analyzed fields: (a) temp (K), (b) water vapor mixing ratio, (c) wind divergence (1.0×10^{-5} s^{-1}), and (d) vertical velocity omega in pressure system (mb h^{-1}).

latent heating and turbulent heating, will be presented in a separate study. In this paper, we focus on the robustness of the objectively analyzed product. To reduce the length of the paper, we will only use the pressure vertical velocity (omega) to examine the data sensitivities. Three sets of experiments are carried. Results will be presented for analyses with mass constraint only and with all constraints of Eqs. (9)–(12). The first set of experiments is designed to test the impact of the interpolation schemes. The second set of experiments is designed to show the sensitivity of the analysis on the availability of input data, including profiler data, sounding data, and RUC output. The third set is to test the sensitivity of the data to the constraint variables in Eqs. (9)–(12) and to the weighting coefficients in the cost function (13).

a. Interpolations

For brevity, we only present results by using the analyses from the Barnes scheme. The omega fields for the July 1995 ARM IOP from the Barnes scheme, analyzed with mass constraint only, are shown in Figs. 10a–c. In Fig. 10a, only one iteration is performed in the Barnes scheme with a four-dimensional length scale of (Lx = 50 km, Ly = 50 km, Lp = 50 mb, Lt = 3 h). Figure 10b is the same except that a larger length scale of (Lx = 100 km, Ly = 100 km, Lp = 50 mb, Lt = 6 hours) is used. Figure 10c is the same as Fig. 10b except with three iterations. Consistent with what can be expected from Figs. 3a–c, much smoother and weaker vertical velocity is produced with a larger length scale, and with less iteration. It is noted that the difference in omega is significant between the analyses (e.g., the intensity of the continuous upward motion after day 212), especially for applications such as evaluation of GCM parameterizations.

Figures 10d–f show analyses of omega corresponding to the same three experiments except with all the constraints of Eqs. (9)–(12) imposed. The analyses of omega in Figs. 10d–f are intrinsically consistent with the surface and TOA measurements of precipitation and energy fluxes. We note that differences still exist between the variational analyses resulted from using different

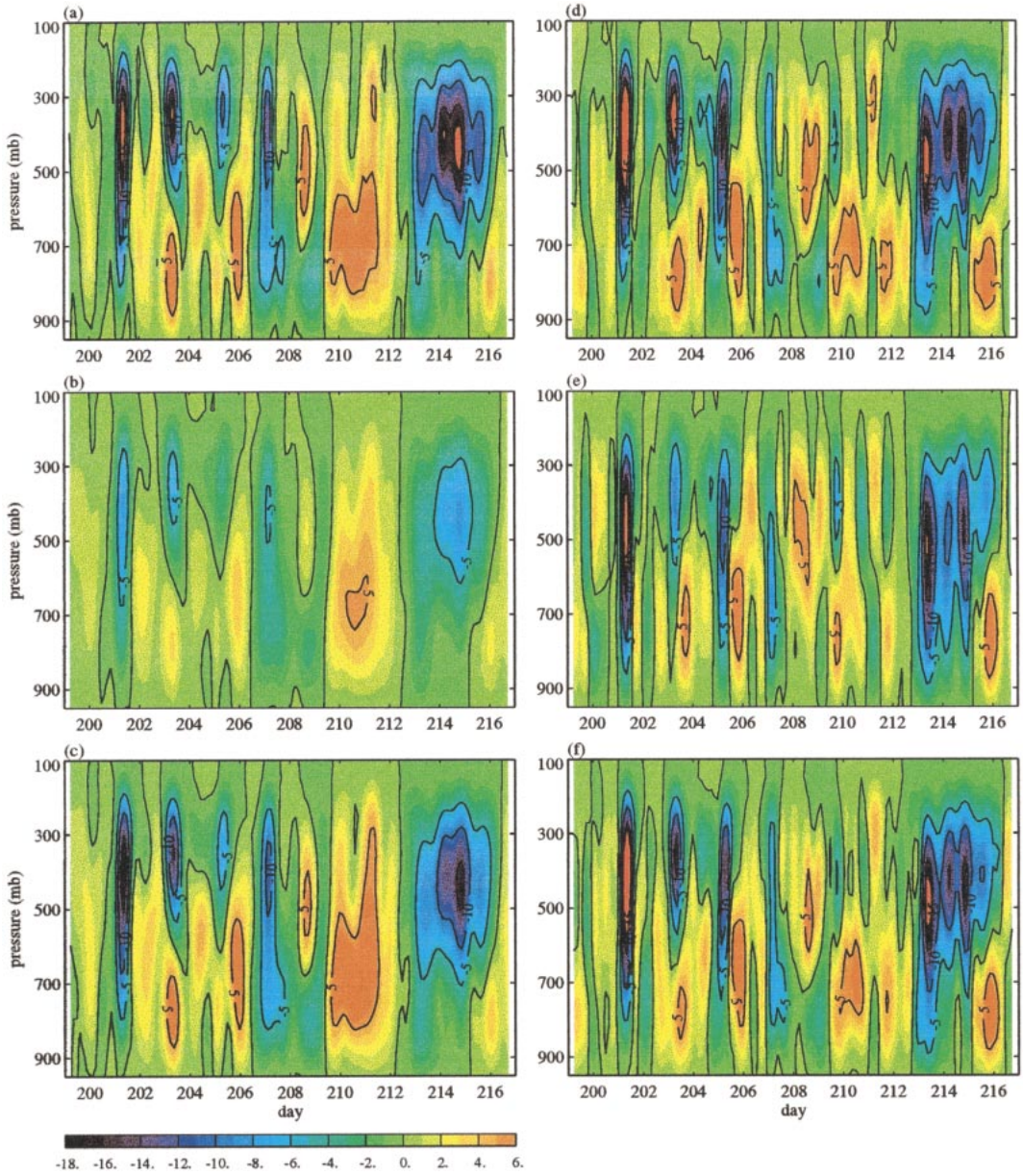

FIG. 10. Sensitivity of the analysis of the pressure vertical velocity omega (mb h^{-1}) to the implementation of the Barnes scheme, with the mass balance constraint only: (a) (Lx, Ly, Lp, Lt) = (50 km, 50 km, 50 mb, 3 h), first iteration; (b) (Lx, Ly, Lp, Lt) = (100 km, 100 km, 50 mb, 6 h), first iteration; and (c) (Lx, Ly, Lp, Lt) = (100 km, 100 km, 50 mb, 6 h), three iterations. (d)–(f) Same as (a)–(c) except with all constraints imposed.

implementation of the Barnes scheme. The use of additional surface and TOA measurements, however, has reduced the sensitivity of the analyses to the interpolation schemes.

b. Data sources

We next experiment with using only sounding data, only profiler data, and the RUC model output as our upper-air data sources. This set of experiment is carried out with two purposes. One is to assess the impact of the input data on the final product, another is to examine the possibility of using alternative upper-air data to replace soundings, which are expensive. Figures 11a–c show the analysis from using (a) sounding data only, (b) profiler data only, and (c) RUC model output, with mass constraint only. Since the profiler data are only available for winds, analyses of temperature and water vapor in Fig. 11b are taken from RUC. It is seen that the analysis from using the RUC model output is quite different from that by using actual data. Events of upward motions in RUC are weak in comparison with

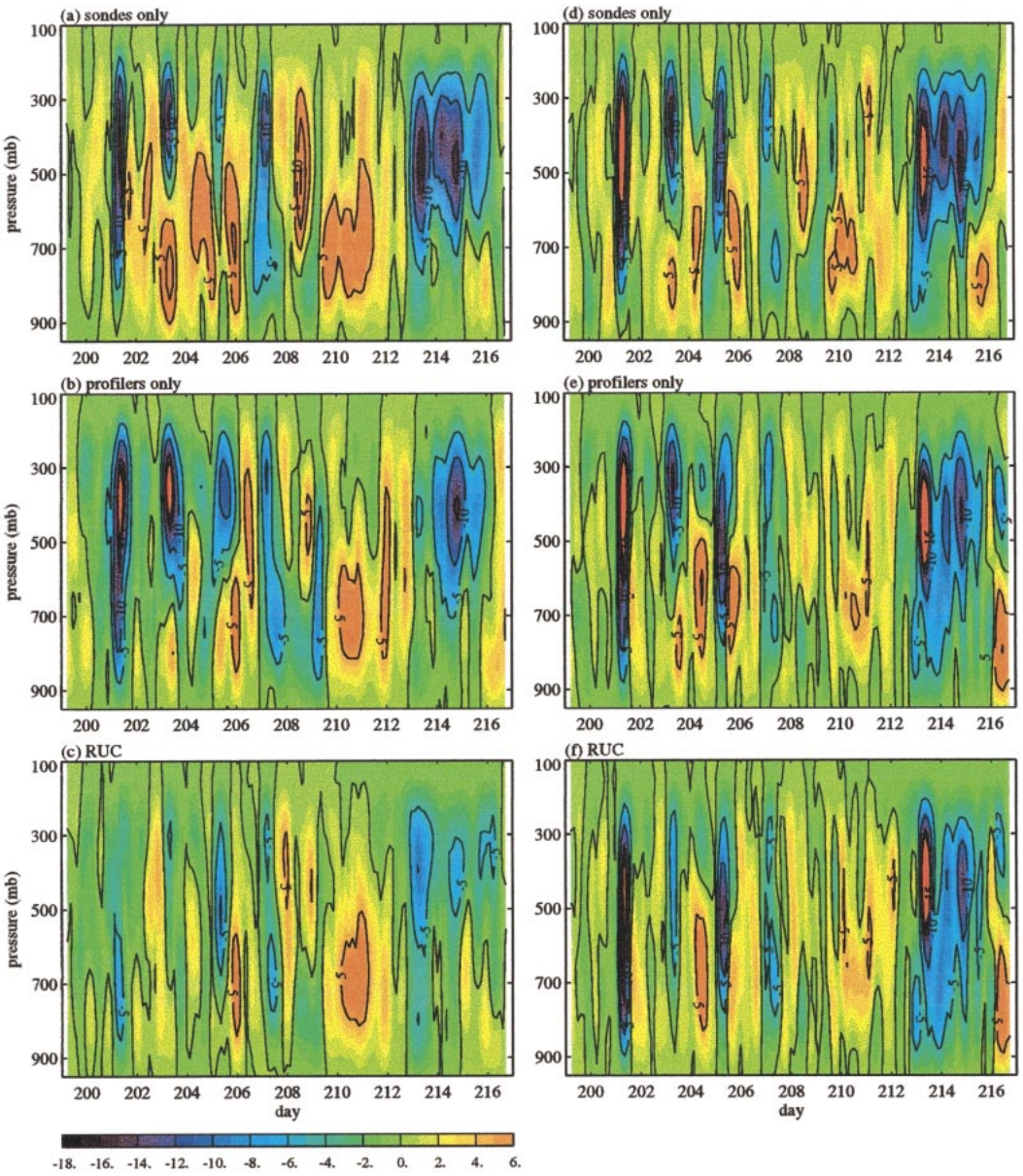

FIG. 11. Sensitivity of the analysis of the pressure vertical velocity omega (mb h^{-1}) to upper-air data sources, with mass balance constraint only: (a) sounding data alone, (b) profiler data alone, and (c) RUC analysis. (d)–(f) Same as (a)–(c) except with all constraints imposed.

those in the other data. The profiler data alone have captured most of the events, except they missed the double peaks from day 213 to day 216. The sounding data displayed the largest variabilities. This is related to the small number of sampling stations.

To better understand what caused these differences among the different data sources, we show a snapshot of vertical–horizontal distribution of winds on day 213 (0530 UTC on 1 Aug 1995) at the ARM SGP in Fig. 12. The first column in the figure shows winds from the five balloon soundings. Wind convergence can be clearly inferred below the 565-mb level, while wind divergence is seen in the top three layers in the figure. The second column shows winds from the profiler stations. It is seen that the profiler winds, wherever available, are in remarkable agreement with the sounding measurements. The profiler winds, however, are missing at the two stations in the north and at the northeast corner. It is seen from the balloon soundings that the winds at the north station are very different from those at the stations to the south and they have contributed to the convergence (divergence) in the sounding data. When the profiler winds are missing at these two stations, an interpolation scheme is used to fill the missing data. Errors are therefore introduced regardless of which interpolation scheme is used.

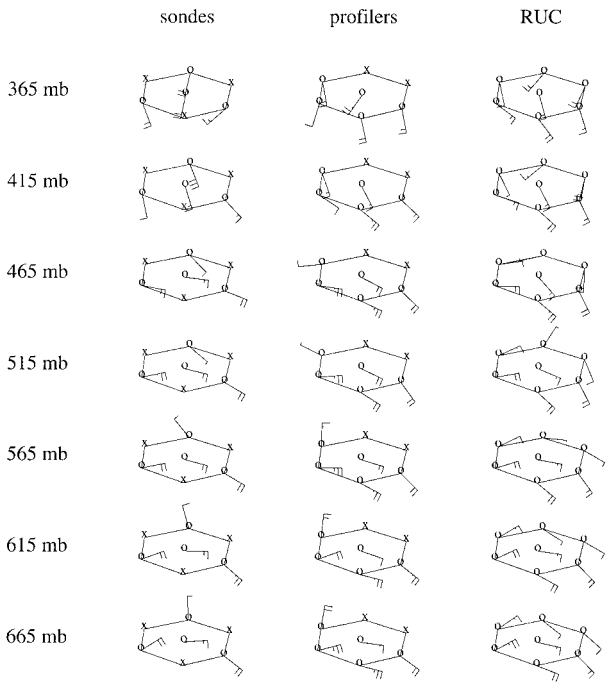

FIG. 12. Vertical–spatial distribution of winds at the ARM SGP at 0530 UTC 1 Aug 1995 (day 213). The first column shows data from the five balloon soundings. The second column shows data from the profilers. The third column shows data from the output of the RUC model.

The third column in Fig. 12 shows the corresponding winds from using the RUC output. It is seen that the RUC winds are generally more homogeneous than those from the actual observations. For example, the wind direction at the station in the north from 565 to 665 mb does not capture the sharp change in the wind direction. This significantly reduces the magnitude of wind convergence as seen in Fig. 11c.

When all constraints are used, the same analyses of omega are shown in Figs. 11d–f. The differences from using the different data sources are reduced. This is particularly true between Figs. 11e and 11f, in which the sounding data and profiler data are separately used. This gives confidence in our finally analyzed data products.

c. Constraint variables and error variances

We now examine the sensitivity of the analysis to the constraining parameters of the variational procedure. We present results from three experiments. In the first experiment, we changed the area-averaged precipitation by using estimates from one-third of the observational stations. The difference in precipitation has been shown in Fig. 6b. We note that characterizing the error uncertainty in the actual precipitation warrants separate study, and here we simply consider the precipitation difference in Fig. 6c as a crude estimate of the uncertainty. In the second experiment, we used the Simple Biosphere Model–(Sib) derived surface latent and sensible heat fluxes as a sensitivity test. These fluxes are plotted in Fig. 6c; they differ significantly from those of the EBBR measurements. Again the difference is considered here as an error estimate in the surface turbulent fluxes. In the third experiment, we change the weights in the cost function of (13) to those used in Zhang and Lin (1997), in which the weights become invariant with height for winds and temperature. In the control case, as described in section 3, the weights were prescribed based on measurement uncertainties and small-scale aliasing calculated from the standard deviations shown in Fig. 8.

Figure 13a shows the analysis of omega when the precipitation is derived from one-third of the observational stations. This omega distribution is very similar to that in the control case in which all precipitation data are used. When we look at the difference field, however, Fig. 13d shows that the intensity of precipitation has a direct impact on the magnitude of the vertical velocity. Stronger precipitation corresponds to stronger upward motion. Yet, the difference is clearly smaller than when using different interpolation schemes.

Figure 13b shows the omega field when the sensible and latent heat fluxes from the EBBR stations are replaced by using those from the Sib model (courtesy of C. Doran, PNNL). Figure 13e shows the difference in vertical velocity from using the different turbulent surface fluxes. Reduction of latent heat flux and increase of sensible heat flux, from using the Sib fluxes, both lead to increased upward motion, since the former would require larger convergence of moisture into the column and therefore stronger upward motion, while the latter requires more divergence of dry static energy and thus stronger divergence in the upper layers. The uncertainty in the analyzed data, however, is seen to be smaller than that from the perturbed precipitation.

We finally show the sensitivity of omega on the choice of the weighting coefficients in the variational cost function (13). Figures 13c and 13f show the analysis of omega and its difference with the control experiment. Unlike the surface constraints, the weighting coefficients change the vertical structure of the analysis. The overall magnitude appears to be smaller than those from other perturbations.

5. Summary and discussion

We have discussed several objective analysis schemes and have shown that considerable differences in the analyzed products exist due to the selection of analysis schemes, and even more so to the actual implementation of a particular scheme. As emphasized in several previous studies (Ooyama 1987; Mace and Ackerman 1996; Parsons and Dudhia 1997), the accuracy of objective analysis of field experimental data is seriously limited by scale aliasings in the measurements. This is particularly important for fields with large subgrid-scale

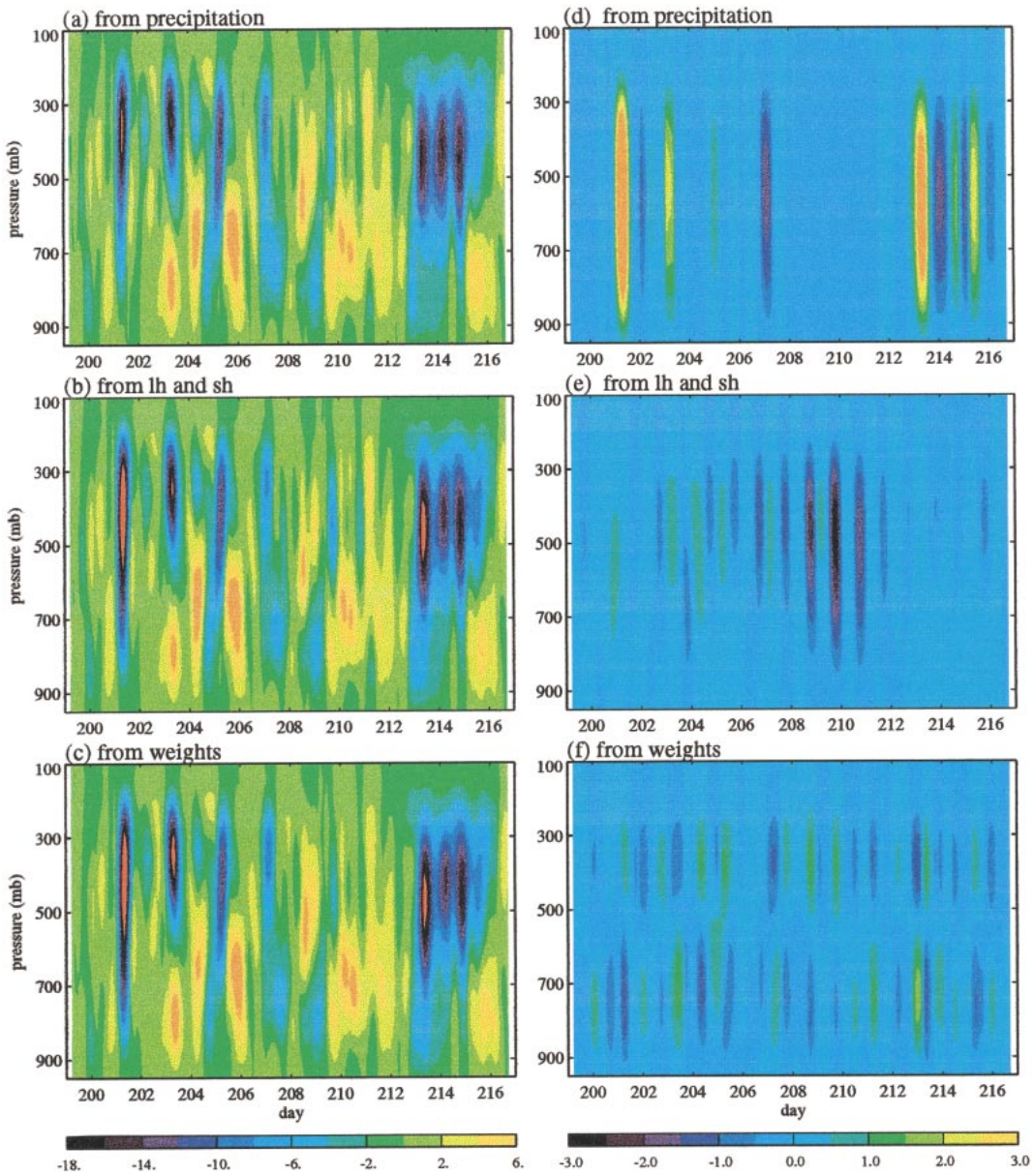

FIG. 13. Sensitivity of the analysis of pressure vertical velocity omega (mb h^{-1}) to parameters in the variational procedure: (a) using precipitation with one-third of the stations sampled, (b) using the SiB latent and sensible heat fluxes, and (c) using pressure-invariant error estimates. (d)–(f) Same as (a)–(c) except for the differences of omega from the control experiment.

variabilities, such as the moisture field, and for events when a severe weather system passes through the measurement network. The only way to fully address the scale aliasing problem is to have sufficient samplings in time and space. This is however practically impossible to achieve.

To alleviate some of these difficulties, we have introduced a hybrid approach to combine the strength of the regular grid method and the line-integral method for the analysis of ARM data, and then subject it to a variational constraining process that ensures the conservation of the column integrated mass, energy, and water vapor budgets. In addition to the use of upper-air data, surface measurements of precipitation, and sensible and latent heat fluxes are all used.

Three sets of experiments are carried out to examine the sensitivity of the analyzed product to the analysis methods and data sources, with and without the column-integrated constraints of water and energy budgets. It is shown that the constraining process significantly reduces the sensitivity of the final data products. It is also shown that uncertainty of the pressure vertical velocity field caused by uncertainties in the variational procedure is smaller than those from using different schemes. In

the constraining process, accuracy of area-averaged precipitation appears to have the largest impact on the data products.

Our approach attempted to use area-averaged and time-averaged constraints to derive the area-averaged quantities. The vertical structures of the derived data, however, are entirely dependent on the original potentially aliased measurements, since the variational analysis is only a least square fit to the available data. It is possible that adjustments at certain stations and altitudes are not necessary but adjustments at other stations and altitudes should be more. Technically, this can be achieved by specifying proper weights in the cost function. Practically these weights are never known.

We envision two directions to further improve the analyzed data. One is to quantify the uncertainties in the analyzed data. It is preferable to include error bars in the analyzed datasets. This is not straightforward, however, because errors in different variables and locations should also be internally constrained by the imposed budgets. An alternative way of characterizing errors is to produce multiple datasets, with each of them internally consistent. This is what we are currently pursuing. The second direction is to improve the sampling of input upper-air data by making more use of remotely sensed data in the interpolation scheme. The missing winds in Fig. 12, for example, have significant impact on the final product. They may be crudely inferred from indirect high spatial resolution satellite measurements such as GOES water vapor and clouds. Additionally, advection of hydrometers should be included in the budget calculations (Petch and Dudhia 1998). These options are being explored. Finally, feedback from the modeling community on the quality of data will be very valuable to the endeavor of improving the objective analysis.

Acknowledgments. We thank the following individuals for numerous discussions in the course of this work: David Randall, Kuanman Xu, Steve Ghan, Chris Doran, Steve Krueger, and James Hack. We thank one of the anonymous reviewers whose comments led us to uncover an initial error and to improvement of the original manuscript. This research is supported by the DOE ARM Program under Grant EFG0298ER62570, and by NSF under Grant ATM901950, to SUNY at Stony Brook. It was also performed under the auspices of the U.S. Department of Energy by the Lawrence Livermore National Laboratory under Contract W-7405-Eng-48. This work was completed when the first author, who wishes to thank Richard Rood, Franco Einaudi, Micheal Kalb, and USRA for their support, visited the Data Assimilation Office at NASA GSFC.

REFERENCES

Barnes, S. L., 1964: A technique for maximizing details in numerical map analysis. *J. Appl. Meteor.,* **3,** 396–409.

Betts, A. K., 1973: A composite mesoscale cumulonimbus budget. *J. Atmos. Sci.,* **30,** 597–610.

Chen, Y.-L., and J. Lin, 1995: Large-scale conditions favorable for the development of heavy rainfall during TAMEX IOP 3. *Mon. Wea. Rev.,* **123,** 2978–3002.

Cotton, W. R., M.-S. Lin, R. L. McAnelly, and C. J. Tremback, 1989: A composite model of mesoscale convective complexes. *Mon. Wea. Rev.,* **117,** 765–783.

Cressman, G. P., 1959: An operational objective analysis scheme. *Mon. Wea. Rev.,* **87,** 367–374.

Daley, R., 1991: *Atmospheric Data Analysis.* Cambridge University Press, 457 pp.

Davies-Jones, R. P., 1993: Useful formulas for computing divergence, vorticity, and their errors from three or more stations. *Mon. Wea. Rev.,* **121,** 713–725.

Esbensen, S. K., 1975: An analysis of subcloud-layer heat and moisture budgets in the western Atlantic trades. *J. Atmos. Sci.,* **32,** 1921–1933.

——, E. I. Tollerud, and J.-H. Chu, 1982: Cloud-cluster-scale circulations and the vorticity budget of synoptic-scale waves over the eastern Atlantic intertropical convergence zone. *Mon. Wea. Rev.,* **110,** 1677–1692.

Frank, W. M., 1979: Individual time period analysis over the GATE ship array. *Mon. Wea. Rev.,* **107,** 1600–1616.

——, H. Wang, and J. L. McBridge, 1996: Rawinsonde budget analyses during TOGA COARE IOP. *J. Atmos. Sci.,* **53,** 1761–1780.

Gallus, W. A., and R. H. Johnson, 1991: Heat and moisture budgets of an intense midlatitude squall line. *J. Atmos. Sci.,* **48,** 122–146.

——, and ——, 1992: The momentum budget of an intense midlatitude squall line. *J. Atmos. Sci.,* **49,** 422–450.

Ghan, S., and Coauthors, 2000: An intercomparison of single column model simulations of summertime midlatitude continental convection. *J. Geophys. Res.,* **105,** 2091–2124.

He, H. Y., J. W. McGinnis, Z. S. Song, and M. Yanai, 1987: Onset of the Asian summer monsoon in 1979 and the effect of the Tibetan Plateau. *Mon. Wea. Rev.,* **115,** 1966–1995.

Johnson, R. H., 1976: The role of convective-scale precipitation downdrafts in cumulus and synoptic-scale interactions. *J. Atmos. Sci.,* **33,** 1890–1910.

——, and G. S. Young, 1983: Heat and moisture budgets of tropical mesoscale anvil clouds. *J. Atmos. Sci.,* **40,** 2138–2147.

——, and J. F. Bresch, 1991: Diagnosed characteristics of precipitation systems over Taiwan during the May–June 1987 TAMEX. *Mon. Wea. Rev.,* **119,** 2540–2557.

Jorgensen, D. P., M. A. LeMone, and J.-D. Jou, 1991: Precipitation and kinematic structure of an oceanic mesoscale convective system. Part I: Momentum transport and generation. *Mon. Wea. Rev.,* **119,** 2638–2653.

Kuo, Y.-H., and R. A. Anthes, 1984a: Accuracy of diagnostic heat and moisture budgets using SESAME-79 field data as revealed by observing system simulation experiments. *Mon. Wea. Rev.,* **112,** 1465–1481.

——, and ——, 1984b: Mesoscale budgets of heat and moisture in a convective system over the central United States. *Mon. Wea. Rev.,* **112,** 1482–1497.

——, L.-S. Cheng, and R. A. Anthes, 1986: Mesoscale analysis of the Sichuan flood catastrophe, 11–15 July 1981. *Mon. Wea. Rev.,* **114,** 1984–2003.

Krueger, S. K. and S. M. Lazarus, 1999: Intercomparison of multiday simulations of convection during TOGA-COARE with several cloud-resolving and single-column models. Preprints, *23d Conf. on Hurricanes and Tropical Meteorology,* Dallas, TX, Amer. Meteor. Soc., 643–647.

Lafore, J.-P., J.-L. Redelsperger, and G. Jaubert, 1988: Comparison between a three-dimension simulation and doppler radar data of a tropical squall line: Transports of mass, momentum, heat, and moisture. *J. Atmos. Sci.,* **45,** 3483–3500.

Leach, M. J., J. Yio, and R. T. Cederwall, 1996: Estimation of errors in objectively analyzed fields and sensitivity to number and spac-

ing of stations. *Proc. Sixth Annual ARM Science Meeting,* San Antonio, TX, DOE CONF-9603149, 149–151.
Lee, C. S., 1989: Observational analysis of tropical cyclogenesis in the western North Pacific. Part II: Budget analysis. *J. Atmos. Sci.,* **46,** 2599–2616.
LeMone, M. A., 1983: Momentum transport by a line of cumulonimbus. *J. Atmos. Sci.,* **40,** 1815–1834.
——, and M. W. Moncrieff, 1994: Momentum and mass transport by convective bands: Comparisons of highly idealized dynamical models to observations. *J. Atmos. Sci.,* **51,** 281–305.
——, G. B. Barnes, and E. J. Zipser, 1984: Momentum flux by lines of cumulonimbus over the tropical oceans. *J. Atmos. Sci.,* **41,** 1914–1932.
Lewis, J. M., 1975: Test of the Ogura–Cho model on a prefrontal squall line case. *Mon. Wea. Rev.,* **103,** 764–778.
Lin, X., and R. H. Johnson, 1994: Heat and moisture budgets and circulation characteristics of a frontal squall line. *J. Atmos. Sci.,* **51,** 1661–1681.
——, and ——, 1996a: Kinematic and thermodynamic characteristics of the flow over the western Pacific warm pool during TOGA COARE. *J. Atmos. Sci.,* **53,** 695–715.
——, and ——, 1996b: Heating, moistening, and rainfall over the western Pacific warm pool during TOGA COARE. *J. Atmos. Sci.,* **53,** 3367–3383.
Lin, Y.-J., T.-C. C. Wang, R. W. Pasken, H. Shen, and Z.-S. Deng, 1990: Characteristics of a subtropical squall line determined from TAMEX dual-Doppler data. Part II: Dynamic and thermodynamic structures and momentum budgets. *J. Atmos. Sci.,* **47,** 2382–2399.
Lord, S. J., and J. L. Franklin, 1990: The environment of Hurricane Debby (1982). Part II: Thermodynamic fields. *Mon. Wea. Rev.,* **118,** 1444–1459.
Luo, H. B., and M. Yanai, 1984: The large-scale circulation and heat sources over the Tibetan Plateau and surrounding areas during the early summer of 1979. Part II: Heat and moisture budgets. *Mon. Wea. Rev.,* **112,** 966–989.
Mace, G. G., and T. P. Ackerman, 1996: Assessment of error in synoptic-scale diagnostics derived from wind profiler and radiosonde network data. *Mon. Wea. Rev.,* **124,** 1521–1534.
McBride, J. L., B. W. Gunn, G. J. Holland, T. D. Keenan, and N. E. Davidson, 1989: Time series of total heating and moistening over the Gulf of Carpentaria radiosonde array during AMEX. *Mon. Wea. Rev.,* **117,** 2701–2713.
McNab, A. L., and A. K. Betts, 1978: A mesoscale budget study of cumulus convection. *Mon. Wea. Rev.,* **106,** 1317–1331.
Miller, B. L., and D. G. Vincent, 1987: Convective heating and precipitation estimates for the tropical South Pacific during FGGE, 10–18 January 1979. *Quart. J. Roy. Meteor. Soc.,* **113,** 189–212.
Minnis, P., W. L. Smith, D. P. Garber, J. K. Ayers, and D. R. Doeling, 1995: Cloud properties derived from GOES-7 for spring 1994 ARM Intensive Observing Period using version 1.0.0 of ARM satellite data analysis program. NASA Ref. Publ. 1366, 59 pp. [Available from NASA Langley Research Center, Technical Library, MS 185, Hampton, VA 23655-5225.]
Nitta, T., 1972: Energy budget of wave disturbances over the Marshall Islands during the years of 1956 and 1958. *J. Meteor. Soc. Japan,* **50,** 71–84.
——, 1977: Response of cumulus updraft and downdraft to GATE A/B-scale motion systems. *J. Atmos. Sci.,* **34,** 1163–1186.
——, and S. Esbensen, 1974: Heat and moisture budget analyses using BOMEX data. *Mon. Wea. Rev.,* **102,** 17–28.
Ooyama, K., 1987: Scale-controlled objective analysis. *Mon. Wea. Rev.,* **115,** 2476–2506.
Parsons, D. B., and J. Dudhia, 1997: Observing system simulation experiments and objective analysis tests in support of the goals of the Atmospheric Radiation Measurement Program. *Mon. Wea. Rev.,* **125,** 2353–2381.
Pedigo, C. B., and D. G. Vincent, 1990: Tropical precipitation rates during SOP-1, FGGE, estimated from heat and moisture budgets. *Mon. Wea. Rev.,* **118,** 542–557.
Petch, J. C., and J. Dudhia, 1998: The importance of horizontal advection of hydrometers in a single column model. *J. Climate,* **11,** 2437–2452.
Randall, D. A., K. M. Xu, R. C. J. Somerville, and S. Iacobellis, 1996: Single-column models and cloud ensemble models as links between observations and climate models. *J. Climate,* **9,** 1683–1697.
Reed, R. J., and E. E. Recker, 1971: Structure and properties of synoptic-scale wave disturbances in the equatorial western Pacific. *J. Atmos. Sci.,* **28,** 1117–1133.
Sanders, F., and K. A. Emanuel, 1977: The momentum budget and temporal evolution of a mesoscale convective system. *J. Atmos. Sci.,* **34,** 322–330.
Song, J.-L., and W. M. Frank, 1983: Relationships between deep convection and large-scale processing during GATE. *Mon. Wea. Rev.,* **111,** 2145–2160.
Stokes, G. M., and S. E. Schwartz, 1994: The Atmospheric Radiation Measurement (ARM) Program: Programmaric background and design of the Cloud and Radiation Test Bed. *Bull. Amer. Meteor. Soc.,* **75,** 1201–1221.
Sui, C.-H., and M. Yanai, 1986: Cumulus ensemble effects on the large-scale vorticity and momentum fields of GATE. Part I: Observational evidence. *J. Atmos. Sci.,* **43,** 1618–1642.
Thompson, R. M., S. W. Payne, E. E. Recker, and R. J. Reed, 1979: Structure and properties of synoptic-scale wave disturbances in the intertropical convergence zone of the eastern Atlantic. *J. Atmos. Sci.,* **36,** 53–72.
Webster, P. J., and R. Lukas, 1992: TOGA COARE: The Coupled Ocean–Atmosphere Response Experiment. *Bull. Amer. Meteor. Soc.,* **73,** 1377–1416.
Wu, X., 1993: Effects of cumulus esemble and mesoscale stratiform clouds in midlatitude convective systems. *J. Atmos. Sci.,* **50,** 2496–2518.
——, and M. Yanai, 1994: Effects of vertical wind shear on the cumulus transport of momentum: Observations and parameterization. *J. Atmos. Sci.,* **51,** 1640–1660.
Yanai, M., and Li, 1994: Mechanism of heating and the boundary layer over the Tibetan Plateau. *Mon. Wea. Rev.,* **122,** 305–323.
——, S. K. Esbensen, and J. H. Chu, 1973: Determination of bulk properties of tropical cloud clusters from large-scale heat and moisture budgets. *J. Atmos. Sci.,* **30,** 611–627.
Zhang, M. H., and J. L. Lin, 1997: Constrained variational analysis of sounding data based on column-integrated conservations of mass, heat, moisture, and momentum: Approach and application to ARM measurements. *J. Atmos. Sci.,* **54,** 1503–1524.